CrossMark

CAMBRIDGE
UNIVERSITY PRESS

Research Paper

Recreating the OSIRIS-REx slingshot manoeuvre from a network of ground-based sensors

Trent Jansen-Sturgeon [1], Benjamin A. D. Hartig [1], Gregory J. Madsen [2], Philip A. Bland [1], Eleanor K. Sansom [1], Hadrien A. R. Devillepoix [1], Robert M. Howie [1], Martin Cupák [1], Martin C. Towner [1], Morgan A. Cox [1], Nicole D. Nevill [1], Zacchary N. P. Hoskins [1], Geoffrey P. Bonning [3], Josh Calcino [4], Jake T. Clark [5], Bryce M. Henson [6], Andrew Langendam [7], Samuel J. Matthews [8], Terence P. McClafferty [9], Jennifer T. Mitchell [7], Craig J. O'Neill [10], Luke T. Smith [11] and Alastair W. Tait [7,12]

[1]School of Earth and Planetary Sciences, Curtin University, GPO Box U1987, Perth, WA 6845, Australia, [2]Lockheed Martin Australia, Barton, ACT 2600, Australia, [3]Research School of Earth Sciences, Australian National University, Canberra, ACT 2601, Australia, [4]School of Mathematics and Physics, The University of Queensland, QLD 4072, Australia, [5]Centre for Astrophysics, University of Southern Queensland, Toowoomba, QLD 4350, Australia, [6]Laser Physics Centre, Research School of Physics and Engineering, The Australian National University, Canberra, ACT 2601, Australia, [7]School of Earth, Atmosphere and Environment, Monash University, Clayton, VIC 3800, Australia, [8]Geological Survey of New South Wales, NSW, Australia, [9]College of Education, Charles Darwin University, Darwin, NT 0909, Australia, [10]Macquarie Planetary Research Centre, Macquarie University, Sydney, NSW 2109, Australia, [11]Department of Earth and Planetary Sciences, Macquarie University, Sydney, NSW 2109, Australia and [12]Biological and Environmental Sciences, University of Stirling, Stirling FK9 4LA, UK

Abstract

Optical tracking systems typically trade off between astrometric precision and field of view. In this work, we showcase a networked approach to optical tracking using very wide field-of-view imagers that have relatively low astrometric precision on the scheduled OSIRIS-REx slingshot manoeuvre around Earth on 22 Sep 2017. As part of a trajectory designed to get OSIRIS-REx to NEO 101955 Bennu, this flyby event was viewed from 13 remote sensors spread across Australia and New Zealand to promote triangulatable observations. Each observatory in this portable network was constructed to be as lightweight and portable as possible, with hardware based off the successful design of the Desert Fireball Network. Over a 4-h collection window, we gathered 15 439 images of the night sky in the predicted direction of the OSIRIS-REx spacecraft. Using a specially developed streak detection and orbit determination data pipeline, we detected 2 090 line-of-sight observations. Our fitted orbit was determined to be within about 10 km of orbital telemetry along the observed 109 262 km length of OSIRIS-REx trajectory, and thus demonstrating the impressive capability of a networked approach to Space Surveillance and Tracking.

Keywords: OSIRIS-REx – networked space situational awareness – Desert Fireball Network – streak detection – triangulation – orbit determination – telemetry comparison – FireOPAL

(Received 25 April 2020; revised 12 September 2020; accepted 15 September 2020)

1. Introduction

Ever since the first Near Earth Object (NEO) was discovered in 1898 (Miller et al. 2002), humanity has been concerned of the threat posed by these objects. A variety of methods have been developed to determine their orbits. NEO orbits can be established using angles-only measurements from a single observation point using Gauss's method (Gauss 1857), Laplace's method (Klokacheva 1991), Gooding's method (Gooding 1997), and/or the Double-R algorithm (Der 2012). However, these single-viewpoint techniques tend to perform better with measurements spanning a large time period.

Modern methods have been developed for the orbit determination of NEO using temporally close measurements that span short arcs, such as the admissible region approach of Milani & Kneevi (2005) and Tommei et al. (2007). However, these methods determine a set of physically acceptable orbits and are still prone to considerable error. An alternative approach to the short-arc problem uses two observatories taking simultaneous measurements to triangulate the NEO, which results in greater accuracy over a shorter time window when compared to the single observatory approach, even when data density is matched. Eggl (2011) describes a method of NEO triangulation using measurements from two heliocentric satellites, and Eggl & Devillepoix (2014) explains the same concept between the Gaia satellite and ground-based observations.

Triangulation has also been used by fireball networks since 1959 to track and dynamically model small NEO from meteor and fireball observations from multiple distributed sensors as they ablate through our upper atmosphere. Of the 60 000 meteorites in collections around the world, only about 32 have known orbits as

of 2018 (Granvik & Brown 2018). Five of these have been discovered using the Desert Fireball Network (DFN), the largest fireball network in the world.

With fireball networks as inspiration, we propose using the same distributed multi-observatory approach to triangulate objects beyond our atmosphere. The question is whether it is possible to accurately determine the orbit of a heliocentric object using many relatively low-resolution ground-based sensors. If this is indeed possible, it would not only allow for advances in the scientific study of NEO, but it would open up a wide range of networked-based observation applications in alternative fields, including Space Surveillance and Tracking (SST).

To answer this question and test the validity of such an approach, we observed the OSIRIS-REx spacecraft's flyby manoeuvre on 22 Sep 2017, using Australasia as our triangulation baseline. Additionally, to verify the accuracy of such a method, we recreate its NEO-like orbit and compare it to well-known orbital telemetry.

2. Observatory hardware

Rapidly deployable proof-of-concept observatories were developed to demonstrate a network-based approach to NEO observation and, by extension, SST by imaging the OSIRIS-REx spacecraft during its flyby manoeuvre. As the chosen observation locations were spread out to very different places across the country, these observatories were constructed to be portable, lightweight, and easy to set up and operate in the field by non-specialists. The design consisted of only the bare-bones components and could be separated into two parts—a small custom-designed triggering unit and the imager itself—all able to be transported in a small case as carry on luggage as shown in Figure 1.

The triggering unit is a key piece of hardware that takes advantage of the DFN's existing hardware (Howie et al. 2017). It contains a micro-controller linked to a Global Navigation Satellite System (GNSS) chip to activate the camera's shutter at predetermined times. The triggering unit also contains an SD card to record the imager's geodetic coordinates and absolute time information for later data processing. The predetermined times were synchronised across the continental-scale network at a cadence of 6 s, triggered to sub-millisecond precision. This synchronisation between observatories allowed for individual pointwise triangulation and possible reconstruction of spacecraft geometry through light curve analysis.

The imager consists of a Nikon D810 36 megapixel DSLR full-frame sensor paired with either a Sigma Art 85 mm f/1.4 (11 observatories) or a Nikon Nikkor 105 mm f/1.4 lens (2 observatories). The Nikon camera was set to 3200 ISO, maximum aperture (f/1.4), and 4 s exposure time.

The majority of these portable observatories provide a $24° \times 16°$ field of view or 385 square degrees, resulting in a resolution of about 11.5 arcsec per pixel. This would be classed as relatively low resolution when compared to a typical SST telescope, such as the Falcon Telescopes (Chun et al. 2018). Sponsored by the United States Air Force Academy (USAFA), the Falcon Telescopes support a 0.5 m, f/8.1 lens, and 0.65 arcsec per pixel, equating to a coverage of only about 12 square degrees. While these typical SST telescopes are fantastic at refining the orbit of an already catalogued space object, they lack the field of view necessary for blind target acquisition and even have trouble capturing targets of high uncertainty, which is where large field-of-view sensors excel.

Figure 1. One of the observatories used in the OSIRIS-REx observation campaign, complete with the custom-designed triggering unit.

3. OSIRIS-REx observation campaign

The site selection and observatory pointing for the observation campaign were both based around the OSIRIS-REx slingshot orbit as predicted by NASA. This predicted orbit was gathered from the NASA Horizons web service (https://ssd.jpl.nasa.gov/horizons.cgi) on 17 Aug 2017, about a month before the flyby manoeuvre.

3.1. Site selection

The optimal triangulation baseline for any target is when observations from two or more observatories meet at 90°. Due to the large range of OSIRIS-REx even at closest approach, this baseline is greater than the diameter of the Earth. Therefore, to best demonstrate the distributed network approach, observatory sites were chosen to maximise the observation baseline while avoiding

Table 1. The final locations of the portable observatories on the night of 22 Sep 2017. The OSIRIS-REx viewing window and number of images captured are also shown for each site. Each observatory supported a 85-mm lens besides two locations (*), which used the 105 mm lens.

Location (Codename)	Latitude	Longitude	Observed window	Collected images
Auckland (AKL)	−35.548°	174.303°	1^h 36^m	546
Canberra (ANU)	−36.522°	149.228°	4^h 06^m	2 147
Alice Springs (ASP)	−23.683°	133.928°	3^h 32^m	1 586
Broken Hill (BHQ)*	−31.847°	141.203°	4^h 15^m	1 564
Darwin (CDU)	−13.044°	130.995°	3^h 35^m	1 398
Darwin (DRW)*	−13.044°	130.995°	3^h 31^m	1 415
Mount Isa (ISA)	−20.903°	139.440°	3^h 38^m	1 535
Kalgoorlie (KGI)	−30.751°	121.760°	3^h 23^m	2 031
Learmonth (LEA)	−22.401°	114.039°	2^h 53^m	1 050
Melbourne (MON)	−36.975°	145.706°	1^h 17^m	719
Sydney (MQU)	−33.536°	151.295°	2^h 30^m	–
Perth (PER)	−32.406°	116.725°	0^h 18^m	139
Toowoomba (USQ)	−27.825°	152.101°	3^h 25^m	1,309

light polluted areas and adverse weather conditions on the night of 22 Sep 2017. As such, 12 sites across Australasia were chosen in advance with a few alterations very last minute depending on the weather forecast.

The portable observatories on these 12 sites were operated by teams from 6 different Australian institutions. A 13th observatory was set up alongside the Darwin node to allow direct performance comparisons between the 85 mm and 105 mm lenses. The final viewing sites for the OSIRIS-REx flyby are shown in Figure 2 and specified in Table 1.

3.2. Pointing

The OSIRIS-REx slingshot trajectory spanned a large fraction of the sky, considerably more than the field of view of our observatories. Therefore, a number of manual re-points were required by the observatory operators over the collection window. This collection window started from about 22 Sep 2017 12:35 UTC, when OSIRIS-REx was predicted to be at our sensor's limiting brightness of 12th magnitude, and finished just before it fell below the horizon over 4 h later. Fortunately, the Moon was set for the entire collection period, giving us the best chance at capturing the faint reflection of the OSIRIS-REx spacecraft.

To avoid frequent re-pointing while still keeping the OSIRIS-REx spacecraft near the centre of the field of view, the predicted altitude/azimuth pointing information was segmented into 5° arcs from each observatory's perspective. The centroid of these arc segments dictated where the sensor was to be pointed and at what time. This resulted in about 25 re-points over the course of 4 h, with an initial spacing of 20 min down to about 4 min by the end as OSIRIS-REx increased in apparent angular velocity as it approached the horizon.

The actual process of pointing the sensors on the night was rough due to the imprecise nature of the compass (corrected for magnetic declination) and an inclinometer used to aim the lens. However, the 5° arc segment was designed to be sufficiently smaller than the field of view of the lens to cater for this known

inaccuracy. This rudimentary pointing method allowed less experienced operators to successfully observe the target, without the need of sky charts or even the need to carry a computer.

3.3. Gathered data

Over the course of the observation campaign, 15 439 images were taken of the night sky from 12 different viewpoints. Observer location and absolute time records were also gathered alongside these images at the moment of shutter actuation using the custom triggering box described in Section 2. The locations and collected data for each observatory are summarised in Table 1.

This is far too much data to be reduced manually. In order to recreate the OSIRIS-REx slingshot orbit from the gathered imagery, an automated data reduction pipeline was required.

4. Recreating the OSIRIS-REx orbit

To construct the flyby orbit of the OSIRIS-REx satellite, we must first detect and extract the start and end points of the recorded spacecraft's streak from the mass of images captured from the various observation sites in a process called streak detection. Additionally, if OSIRIS-REx is visible, light curves can be determined throughout the manoeuvre from different points of view.

Using the extracted streak information from the images, we determine the most likely orbit of the OSIRIS-REx spacecraft given the mass of measurements. This recreated orbit fit is then compared to both NASA Horizons predicted path and actual OSIRIS-REx telemetry of the flyby trajectory.

4.1. Streak detection

Of the 15 439 captured images, the OSIRIS-REx spacecraft was detected in 1 045 of them from 9 viewpoints. Unfortunately, the data collected from four of the locations were unusable due to technical- or weather-related issues. Additionally, out of the sites that did capture valuable imagery, OSIRIS-REx was not observed in all of them because of either human pointing error, unfavourable lighting, or OSIRIS-REx was simply too faint to detect. For streak scale, Figure 3 shows an OSIRIS-REx streak detection in a full-framed image.

To autonomously extract the OSIRIS-REx streak information from the images, we designed a sensitive streak detection algorithm. Firstly, adjacent images captured from the same sensor are astrometrically aligned, smoothed, and subtracted from one another to highlight any differences. The smoothly varying background sky is then removed before any statistically significant streaks are identified. Thumbnails centred around these streaks are saved, with the encompassed stars used to astrometrically and photometrically calibrate the target streaks. Two examples of OSIRIS-REx thumbnails are shown in Figure 4, with the streak itself highlighted.

By tuning the streak detection algorithm towards sensitivity, we introduce a significant number of noise-level artefacts. However, most of these artefacts can be discarded as they do not resemble a satellite streak or they are not in the predicted region of the image to be OSIRIS-REx. The OSIRIS-REx search region within each images is large enough to cater for any inaccuracies in the predicted trajectory but small enough to avoid most of the aforementioned artefacts.

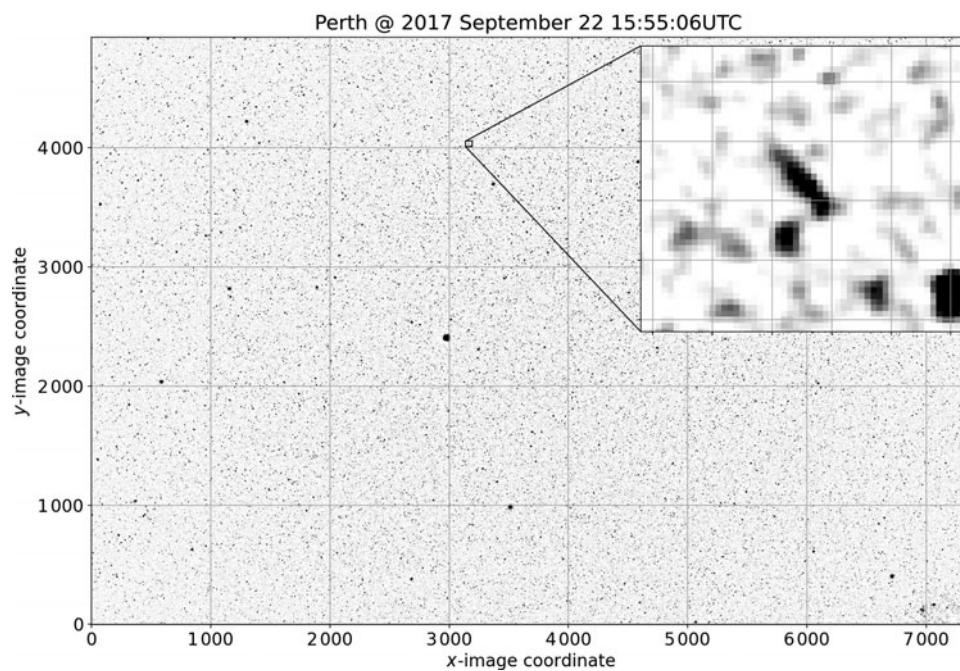**Figure 2.** Sensor locations on the night of the OSIRIS-REx slingshot manoeuvre.

Figure 3. An example of a full-framed image with an enlarged region to show the scale of an OSIRIS-REx streak. For reference, this image is 24° × 16°.
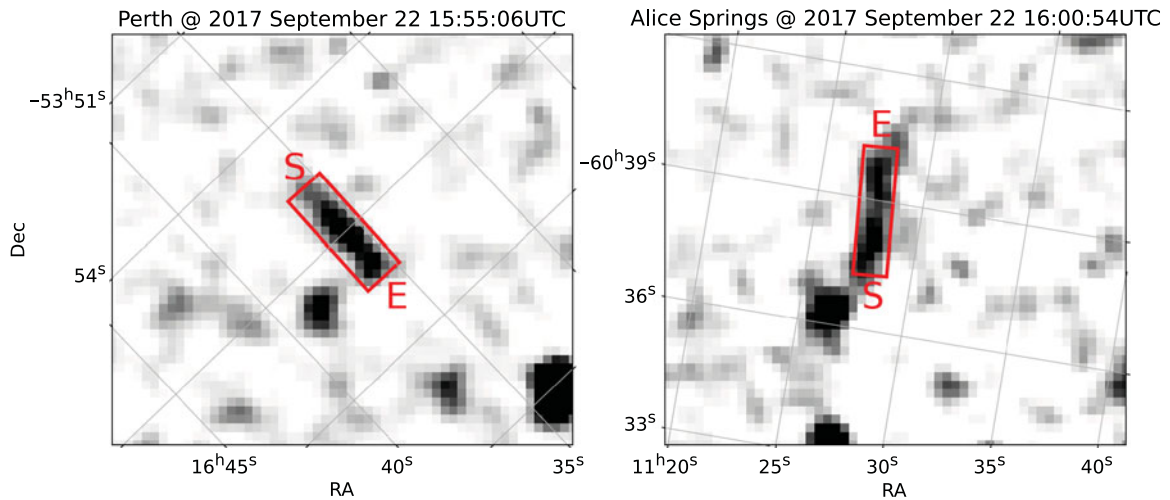
Figure 4. Two thumbnail examples of OSIRIS-REx within 4-s-long exposures as viewed from Perth and Alice Springs, respectively. The OSIRIS-REx streak has been highlighted and its direction of travel indicated, where 'S' is the start and 'E' is the end of the exposure. The full-frame image had been astrometrically calibrated before thumbnail creation.
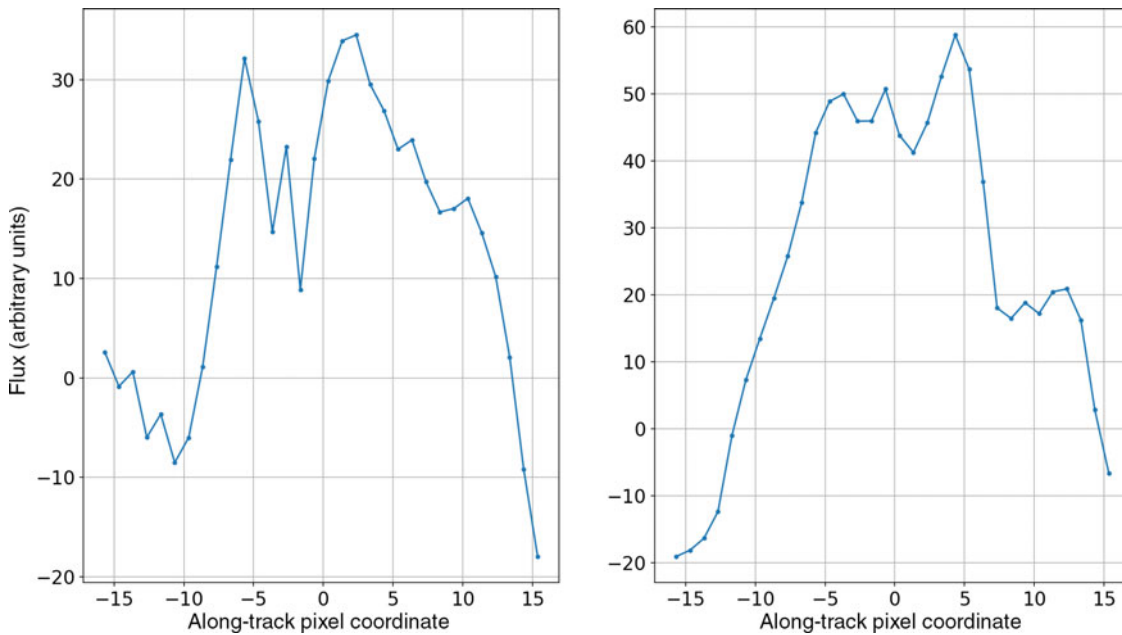

Figure 5. The flux measured along the OSIRIS-REx streaks corresponding to those highlighted in Figure 4, where the zeroth pixel coordinate coincides to the middle of the streak.

Generally, a streak's direction of travel can be identified by comparing it to past and future images from the same sensor. However, sometimes streaks do not appear in the adjacent images, making the streak's orientation ambiguous. Due to the faintness of OSIRIS-REx, the streak detection algorithm detected a significant number of ambiguous streaks. This ambiguity is later resolved at the orbit determination stage.

4.2. Light curves

After a streak has been identified and measured as described in Section 4.1, the light curves are then determined by examining the pixel brightness along the length of the streak. The pixel brightness is converted into apparent flux along the streak using the photometric calibration obtained in the streak detection step.

These simultaneous light curves gathered from various synchronised viewpoints would allow for the complete reconstruction of the OSIRIS-REx spacecraft's geometry. Figure 5 shows how the brightness changes within a couple of example streaks and Figure 6 shows OSIRIS-REx's change in apparent magnitude over the flyby viewing window from all perspectives.

Perhaps surprisingly, the apparent magnitude of the OSIRIS-REx spacecraft begins relatively bright, becoming its dimmest about 2 h before the closest approach. One might think that the brightness of the spacecraft should increase monotonically as the observation range decreases. This would be true if all other factors were ignored, such as the satellite's orientation, irregular shape, varying albedo, and in particular phase angle. The phase angle of OSIRIS-REx throughout the observation campaign went from 15° to over 90°, where 0° corresponds to maximum solar reflectance.
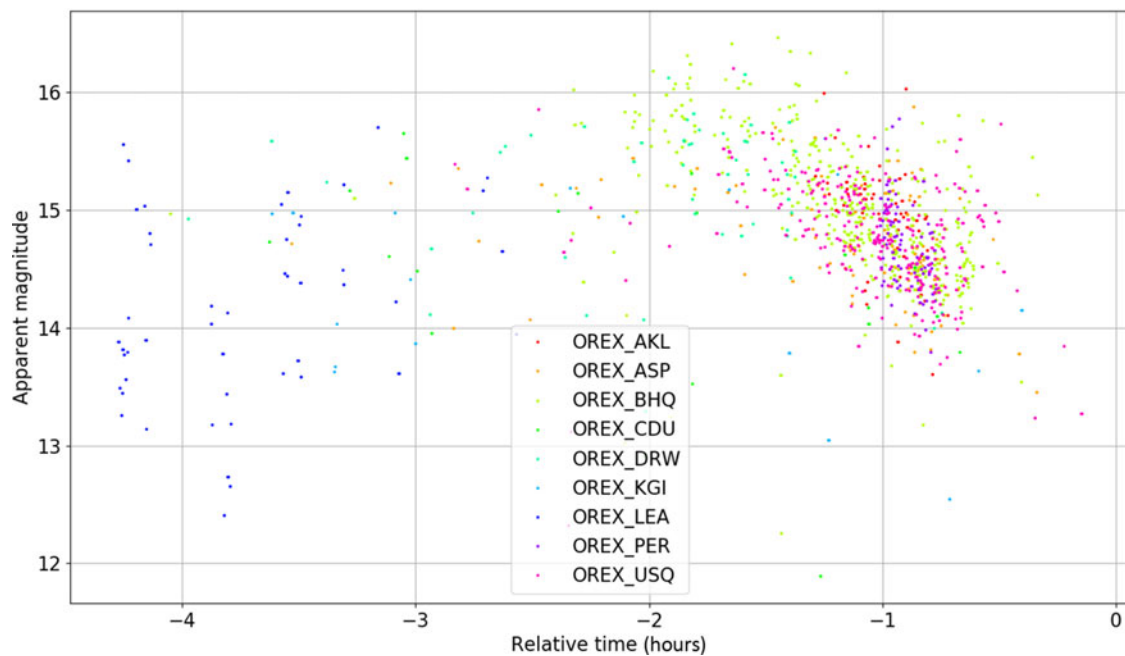
Figure 6. Apparent magnitude of the OSIRIS-REx spacecraft from different observation locations throughout the observation campaign. Times are relative to the closest approach; 22 Sep 2017 16:51:50.818 UTC. See Figure 2 for the specific sensor locations.

Additionally, the spread of these apparent magnitudes as shown in Figure 6 can be due to a multitude of reasons, including Sun glint off the solar panels, complex geometry of the satellite, and locally varying atmospheric conditions.

4.3. Orbit determination

Calculating an orbit given all the line-of-sight measurements is merely an optimisation/fitting problem. To determine this best fit orbit, we choose to use a batch least-squares approach that iteratively adjusts an initial orbit guess (comprising of six orbital parameters) to minimise the sum of the squared residuals, where in our case, a residual is the angular difference between the observed line of sight and the predicted line of sight at the time of the observation. The predicted lines of sight are calculated from the initial orbit guess using a two-body Earth-centred (J2000) hyperbolic orbit propagator due to the nature of the flyby event.

This least-squares minimisation procedure is repeated until a local minimum is reached as determined by the residual Jacobian. If any residuals are outside three median absolute deviations at the point of this local minimum, they are classed as outliers and are removed one by one before the batch least-squares procedure is re-run on the remaining data. An outlier could unavoidably arise during the image differencing step within the streak detection algorithm if an observed OSIRIS-REx streak occultates a star, for example. This outlier rejection step is repeated after every least-squares operation until no outliers remain to contribute to the optimal orbit fit.

In late 2018 at the AMOS conference, a preliminary orbit fit was presented using the above procedure that merely used the centroids of the streaks (Jansen-Sturgeon et al. 2018 and therefore did not require any ambiguous streak handling as mentioned in Section 4.1. In order to include all avaliable line-of-sight measurements, the orbit determination algorithm was later refined to use the start and end pointing coordinates of the OSIRIS-REx streaks.

Table 2. The hyperbolic orbital elements at the time of closest approach, 22 Sep 2017 16:51:50.818 UTC, expressed in the Earth-centred inertial (GCRS) coordinate frame. In order, p, e, i, ω, Ω, and M correspond to the perigee, eccentricity, inclination, argument of perigee, longitude of the ascending node, and the mean anomaly, respectively.

Orbital elements	Horizons prediction[a]	Determined orbit	Orbit telemetry[b]
p (km)	23 595.52402	23 590 ± 8	23 591.78261
e	3.29654	3.2971 ± 0.0006	3.29620
i (°)	84.84226	84.831 ± 0.001	84.83158
ω (°)	284.52092	284.528 ± 0.004	284.52307
Ω (°)	185.61554	185.606 ± 0.001	185.61538
M (°)	0.18841	0.180 ± 0.004	0.15535

[a] Gathered from NASA Horizons Web-Interface on 17 Aug 2017.
[b] Gathered from NASA Horizons Web-Interface post slingshot.

To combat the streak ambiguity problem, the ambiguous streak's direction of travel is determined before any optimisation techniques are applied by comparing to the known NASA Horizons predicted orbit. Any ambiguous streaks that appear to be heading in the wrong direction are flipped, that is, if their dot product with the projected velocity vector at that time is less than zero. This streak flipping process ultimately aids in the accuracy of the overall orbit fit.

The adjusted orbit determination code corrected 198 of the 353 ambiguous streaks that were found to be oriented the wrong way. Additionally, we identified 99 out of the 2 090 measurements as outliers, which were discarded from the final orbit fit. The remaining measurements are represented in Figure 7 as the orbit residuals, and the final calculated hyperbolic orbital elements are listed in Table 2.

To validate the use of this simple two-body approximation, we calculate the deviation from the strongest perturbation (namely J_2)
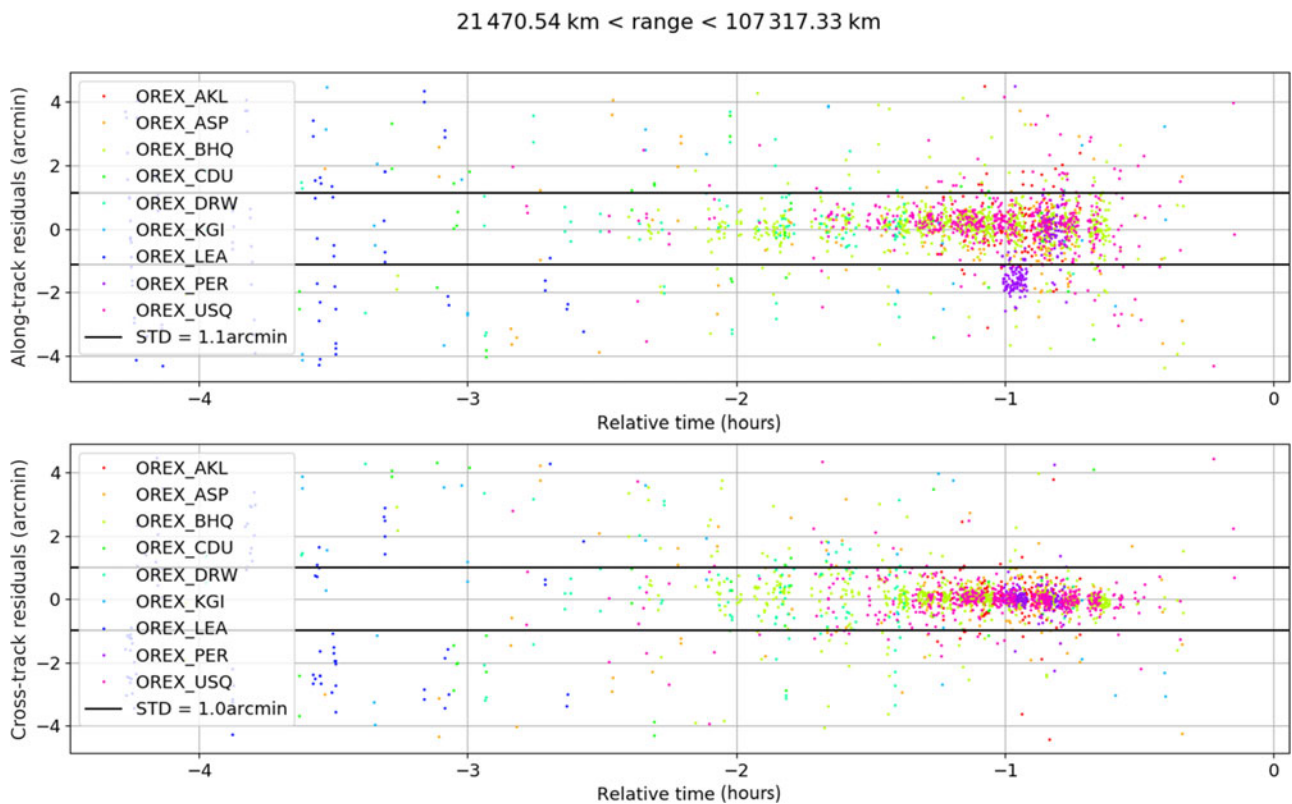
Figure 7. The angular difference between the observed line-of-sight measurements and the predicted lines of sight over time given the fitted hyperbolic orbit, otherwise known as residuals. The sensors are colour-coded and the residual standard deviation is given in black. The time is relative to the point of closest approach; 22 Sep 2017 16:51:50.818 UTC.

over our 4 h observation window to be about 30 m. This is far less than the error on the perigee alone, see Table 2, and therefore would negligibly affect our overall orbit solution.

4.4. Orbit comparison

Now that we have calculated OSIRIS-REx's orbital trajectory, and we have an opportunity to compare this against the original predicted orbit and actual OSIRIS-REx telemetry. As discussed, the predicted orbit was gathered from NASA Horizons web service (https://ssd.jpl.nasa.gov/horizons.cgi) on 17 Aug 2017, about a month before the flyby event. The orbital telemetry was collected from the same location about a year after the event and has not been altered since. Table 2 compares the hyperbolic orbital elements of the determined orbit to the prediction and telemetry orbits, while Figure 8 compares them all visually.

As shown in Figure 8, the three orbits are so close to one another that they are practically indistinguishable at this scale. Likewise, comparing the numbers directly from Table 2 can be misleading and does not show the subtle differences between them. In order to visualise the subtle variation between these orbits, we investigate the cross-track differences to the telemetry by constructing a frame of reference centred around and travelling with the telemetry trajectory, as shown in Figure 9. This telemetry 'body frame' approach highlights the slight orbit differences throughout the flyby trajectory, where points in the body's x-y frame (Figure 9) represent parallel trajectories.

Figure 9 shows how parallel the Horizons predicted trajectory is to the orbital telemetry as indicated by the relatively small deviation over the 12 h window. Additionally, we note how

accurate the determined orbit is to the telemetry, with only about 4 h of measurements using human pointed off-the-shelf cameras.

Interestingly, if we use the observation range to convert the angular cross-track residual standard deviation into an equivalent residual distance, we get a linear cross-track residual standard deviation of about 31.2 km and 6.2 km corresponding to the start and the end of the observation window respectively, well within one standard deviation of the telemetry orbit, that is, the x-axis of Figure 9.

5. The creation of FireOPAL

The OSIRIS-REx observation campaign turned out to be an excellent proof of concept for a networked design for SST. As demonstrated in Section 4.4, we were able to successfully recreate a NEO-like orbit using a distributed network of relatively low-resolution off-the-shelf imagers. Additionally, this achievement proved the capability of the developed and automated data reduction pipeline. To expand this successful proof of concept into the observation of Earth-bound objects and space debris, the prototype hardware, observatory structure, and data pipeline were adjusted into a more durable SST system now known as FireOPAL, a partnership project between Curtin University and Lockheed Martin, Australia.

Perhaps the biggest modification in the development of FireOPAL (Fireball OPtical ALert) was made to the observatory hardware. Each observatory is now completely autonomous and weather-hardened, consisting of a stand-alone and sturdy fixed-pointing sensor, four large solar panels, a set of high-capacity
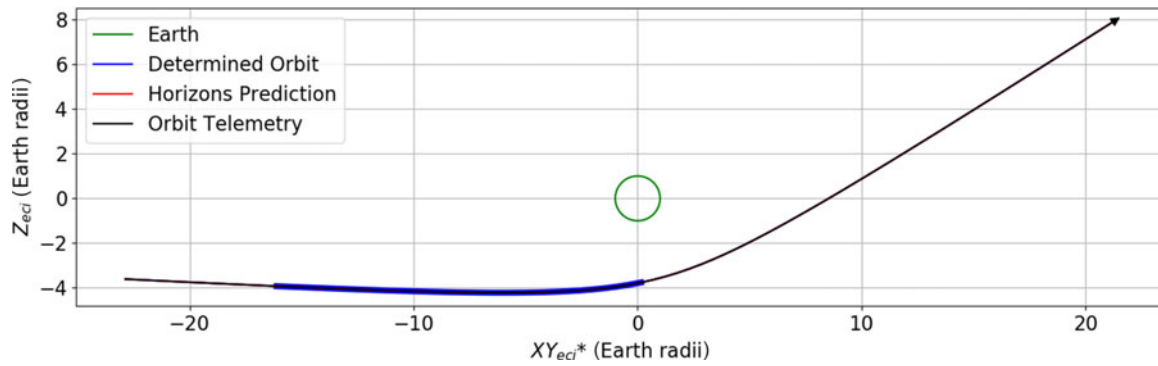
Figure 8. The three hyperbolic orbits from Table 2 compared in the Earth-centred inertial (GCRS) frame, spanning 6 h either side of the closest approach. The orbits are so similar that they appear as one orbit in this plot. To visualise the subtle orbit differences, please refer to Figure 9. The thicker blue trajectory is highlighting the 4-h-long observed section of the determined orbit. *The XY_{eci} axis is angled at an azimuth equal to the longitude of ascending node of the determined orbit as to best represent the hyperbolic orbits in a 2D plane.
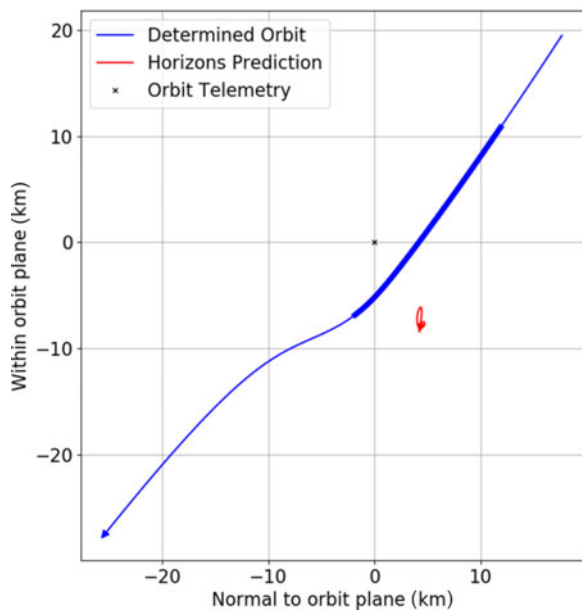

Figure 9. The subtle cross-track differences of the Horizons predicted trajectory and the determined orbit to the telemetry trajectory. The z-axis (into the page) and the y-axis correspond to the direction of the telemetry's velocity vector and the direction of Earth, respectively. The observed section of the determined orbit is highlighted by a thicker blue line. For reference, the distance travelled along the z-axis of this plot is 109 262 km, further enforcing how similar these orbits are.

batteries, and an on-board computer to perform streak determination and light curve extraction remotely and automatically in the field. The comparison of the 85 and 105 mm lenses during the OSIRIS-REx campaign ultimately influenced our choice to use the 105 mm lens in the FireOPAL units due to its increased sensitivity. For reference, Figure 10 shows two FireOPAL observatories deployed in Glendambo, South Australia.

These fixed-pointing sensors are arranged and aligned to maximise the number of recorded satellites from all orbit regimes, with overlap that enables triangulation for more accurate orbit determination. Currently, there are three clusters at different longitudes across Australia that each comprise of 6+ sensors tiling the Geosynchronous Earth Orbit (GEO) belt like a 'fence'. Sufficiently large satellites and space debris that pass through this field of view during the terminator window are observed by the network.
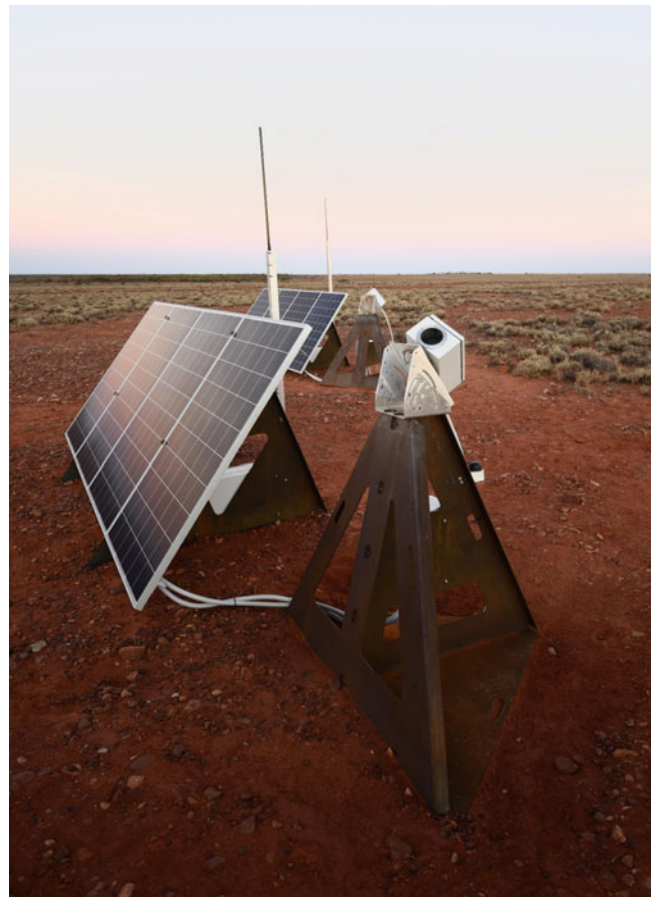

Figure 10. Two current FireOPAL units deployed at Glendambo that are part of six within South Australia. These six observatories form one node that tiles the GEO belt, with two additional similar nodes located in Western Australia and New South Wales.

The OSIRIS-REx streak detection and light curve extraction algorithms have been adjusted to minimise noise-level artefacts while maintaining the majority of true positive detections. A complete account of the FireOPAL image processing pipeline is detailed by Madsen et al. (2018). Additionally, the orbit determination algorithm used in the calculation of OSIRIS-REx's slingshot trajectory has also evolved into a fully autonomous

data association and orbit determination/refinement pipeline (Jansen-Sturgeon 2019). Ambiguous streak directions are now automatically determined within the data association modules. Furthermore, the hyperbolic orbit propagation module was swapped out for the high-fidelity OreKit propagator (Maisonobe, Pommier, & Parraud 2010) to improve the accuracy of the estimated satellite orbits.

In late 2018, Madsen et al. (2018) revealed the first results of the FireOPAL network. These systems were shown to record about 4 000 images a night, detecting around 1 500 Low Earth Orbit (LEO) streaks and 1 000 GEO measurements down to limiting magnitudes of 13.7 mag (single frame) and 16.6 mag (60 stacked frames), respectively. When comparing the GEO measurements from one clear night to known objects in the SpaceTrack catalogue, FireOPAL was found to have a 90% detection rate of targets within an observatory's field of view, with no bias to size.

Madsen et al. (2018) also reported successful collaborative hand-off experiments of LEO and GEO satellites to a narrow field-of-view telescope operated by the Australian Defence Science & Technology Group (DST) 24 h after their latest viewing. This hand-off relied on the fully autonomous orbit determination and refinement pipeline to both construct the orbits and predict the future locations of a number of satellite objects. Over 90% of the hand-off objects were detected by the DST sensor over a 2-week period in June 2018. For more FireOPAL performance and results, please refer to Bland et al. (2018) and Madsen et al. (2018).

At our current rate of data accumulation over the 21 nodes within FireOPAL network, we expect to record over 7 million LEO streaks and over 5 million GEO observations in 1 yr. These numbers only set to increase in the future when more FireOPAL sensors are distributed at different longitudes around the world, leading to an SST network capable of high satellite custody, making it far easier to detect and follow satellites through orbital manoeuvres. Working together with existing SST radar and telescope instruments, FireOPAL will aid greatly in collision avoidance and overall space traffic management in an effort to avoid the potential Kessler event (Kessler & CourPalais 1978).

6. Conclusion

Using a distributed network of relatively low-resolution ground-based off-the-shelf sensors, we were able to successfully detect and determine the NEO-like orbit of NASA's OSIRIS-REx spacecraft on its scheduled slingshot trajectory around Earth. On the night of 22 Sep 2017, 13 teams from 6 Australian institutions spread across Australia and New Zealand to optimise triangulation capacity. In all, the observation campaign generated over 13 000 images within about 4 h.

As manual reduction of this dataset was unfeasible, an automated streak detection and orbit determination pipeline was developed. The streak detection algorithm found 1 045 faint OSIRIS-REx streaks, equating to 2 090 line-of-sight measurements, 99 of which were discarded as outliers. The recreated orbit of OSIRIS-REx was within about 10 km of orbit telemetry and closer than the predicted flyby orbit of a month before.

Following the successful result of the OSIRIS-REx observation campaign, the FireOPAL project was initiated to transform this proof of concept into a more permanent SST observation network. With this distributed network approach to SST, we can now

achieve both a high astrometric precision with a large field-of-view sensor, thereby removing the trade-off faced by traditional single-sensor designs.

References

Bland, P., et al. 2018, FireOPAL: Toward a Low-Cost, Global, Coordinated Network of Optical Sensors for SSA, 14, September 2018. URL http://adsabs.harvard.edu/abs/2018amos.confE..14B.

Chun, F. K., et al. 2018, A New Global Array of Optical Telescopes: The Falcon Telescope Network. PASP, 130, 0 095003. ISSN 1538-3873. doi: 10.1088/1538-3873/aad03f. URL https://doi.org/10.1088%2F1538-3873%2Faad03f.

Der, G. 2012, New Angles-only Algorithms for Initial Orbit Determination, 53, September 2012. URL http://adsabs.harvard.edu/abs/2012amos.confE.53D.

Eggl, S. 2011, Refinement of Near Earth Asteroids orbital elements via simultaneous measurements by two observers. CMDA, 109, 211. ISSN 1572-9478. doi: 10.1007/s10569-010-9323-1. URL https://doi.org/10.1007/s10569-010-9323-1.

Eggl, S., & Devillepoix, H. 2014, On the prospects of Near Earth Asteroid orbit triangulation using the Gaia satellite and Earth-based observations. arXiv:1409.5398 [astro-ph], Sept. 2014. URL http://arxiv.org/abs/1409.5398. arXiv:1409.5398.

Gauss, C. F. 1857, Theory of the Motion of the Heavenly Bodies Moving about the Sun in Conic Sections: A Translation of Gauss's "Theoria Motus". With an Appendix. Little, Brown and Company. Google-Books-ID: 1TIAAAAAQAAJ.

Gooding, R. H. 1997, A new procedure for the solution of the classical problem of minimal orbit determination from three lines of sight. CMDA, 66, 387. ISSN 0923-2958, 1572–9478. doi: 10.1007/BF00049379. URL http://link.springer.com/article/10.1007/BF00049379.

Granvik, M., & Brown, P. 2018, Identification of meteorite source regions in the Solar System. Icar, 311, 271. ISSN 00191035. doi: 10.1016/j.icarus.2018.04.012. URL http://arxiv.org/abs/1804.07229. arXiv:1804.07229.

Howie, R. M., et al. 2017, How to build a continental scale fireball camera network. ExA, 43, 237. ISSN 1572-9508. doi: 10.1007/s10686-017-9532-7. URL https://doi.org/10.1007/s10686-017-9532-7.

Hunter, J. D. 2007, Matplotlib: A 2D Graphics Environment. CSE, 9, 90. ISSN 1521-9615. doi: 10.1109/MCSE.2007.55.

Jansen-Sturgeon, T. 2019, Autonomous Triangulation and Dynamic Modelling of Uncooperative Space Objects using a Distributed Network of Remote Sensors. Thesis, Curtin University. URL https://espace.curtin.edu.au/handle/20.500.11937/80105. Accepted: 2020-07-22T01:34:54Z.

Jansen-Sturgeon, T., et al. 2018, FireOPAL: Continental-scale Coordinated Observations of the OSIRIS-Rex Flyby, 45, Sept. 2018. URL http://adsabs.harvard.edu/abs/2018amos.confE.45J.

Kessler, D. J. & CourPalais, B. G. 1978, Collision frequency of artificial satellites: The creation of a debris belt. JGRSP, 83, 2637. ISSN 2156-2202. doi: 10.1029/JA083iA06p02637. URL https://agupubs.onlinelibrary.wiley.com/doi/abs/10.1029/JA083iA06p02637.

Klokacheva, M. Y. 1991, Determination of a Preliminary Orbit by the Laplace Method. SvA, 35, 428. ISSN 0038-5301. URL http://adsabs.harvard.edu/abs/1991SvA....35..428K.

Madsen, G., et al. 2018, FireOPAL: Technical Performance and First Results. URL https://amostech.com/TechnicalPapers/2018/Poster/Madsen.pdf.

Maisonobe, L., et al. 2010, Orekit: an Open Source library for operational flight dynamics applications, 2.

Milani, A., & Kneevi, Z. 2005, From Astrometry to Celestial Mechanics: Orbit Determination with Very Short Arcs. CMDA, 92, 1–18. ISSN 1572-9478. doi: 10.1007/s10569-005-3314-7. URL https://doi.org/10.1007/s10569-005-3314-7.

Miller, J. K. et al. 2002, Determination of Shape, Gravity, and Rotational State of Asteroid 433 Eros. Icar, 155, 3. ISSN 0019-1035. doi: 10.1006/icar.2001.6753. URL http://www.sciencedirect.com/science/article/pii/S0019103501967533.

The Astropy COLLABORATION, et al. 2013, Astropy: A Community Python Package for Astronomy. July 2013. doi: 10.1051/0004-6361/201322068. URL https://arxiv.org/abs/1307.6212.

Tommei, G., et al. 2007, Orbit determination of space debris: admissible regions. CMDA, 97, 289. ISSN 0923-2958, 1572-9478. doi: 10.1007/s10569-007-9065-x. URL http://link.springer.com/article/10.1007/s10569-007-9065-x.